

# Energy & Environmental Science

Accepted Manuscript



This is an *Accepted Manuscript*, which has been through the Royal Society of Chemistry peer review process and has been accepted for publication.

*Accepted Manuscripts* are published online shortly after acceptance, before technical editing, formatting and proof reading. Using this free service, authors can make their results available to the community, in citable form, before we publish the edited article. We will replace this *Accepted Manuscript* with the edited and formatted *Advance Article* as soon as it is available.

You can find more information about *Accepted Manuscripts* in the [Information for Authors](#).

Please note that technical editing may introduce minor changes to the text and/or graphics, which may alter content. The journal's standard [Terms & Conditions](#) and the [Ethical guidelines](#) still apply. In no event shall the Royal Society of Chemistry be held responsible for any errors or omissions in this *Accepted Manuscript* or any consequences arising from the use of any information it contains.

## ARTICLE

Cite this: DOI:  
10.1039/x0xx000000x

Received 00th January 2012,  
Accepted 00th January 2012

DOI: 10.1039/x0xx000000x

www.rsc.org/

## Insights into the catalytic activity and surface modification of MoO<sub>3</sub> during the hydrodeoxygenation of lignin-derived model compounds into aromatic hydrocarbons under low hydrogen pressures

Teerawit Prasomsri, Manish Shetty, Karthick Murugappan and Yuriy Román-Leshkov\*

*Department of Chemical Engineering, Massachusetts Institute of Technology, Cambridge MA, 02139  
E-mail: yroman@mit.edu*

MoO<sub>3</sub> is an effective catalyst for the hydrodeoxygenation (HDO) of lignin-derived oxygenates to generate high yields of aromatic hydrocarbons without ring-saturated products. The catalyst is selective for the C–O bond cleavage under low H<sub>2</sub> pressures ( $\leq 1$  bar) and temperatures ranging from 593 to 623 K. A bond-dissociation energy analysis of relevant phenolic C–O bonds indicates that the bond strengths follow an order of Ph–OH > Ph–OMe > Ph–O–Ph > Ph–O–Me. However, for all model compounds investigated, the MoO<sub>3</sub> catalyst preferentially cleaves phenolic Ph–OMe bonds over weaker aliphatic Ph–O–Me bonds. Characterisation studies reveal that the catalyst surface undergoes partial carburisation as evidenced by the presence of oxycarbide- and oxycarbohydride-containing phases (i.e., MoO<sub>x</sub>C<sub>y</sub>H<sub>z</sub>). The transformation of bulk phases and the surface modification of MoO<sub>3</sub> by carbon/H<sub>2</sub> are investigated to understand the role of surface carbon in the stabilisation and enhanced activity of the partially reduced MoO<sub>3</sub> surface.

### Broader context

The global economy is anticipated to grow four-fold by 2050 and energy demand is projected to increase by 56% between 2010 and 2040.[1,2] Currently, most energy-consuming sectors, especially the transportation sector, rely heavily on non-renewable fossil-based fuels to meet their energy requirements. Not only are fossil fuels undergoing fast depletion, but also their use results in the emission of greenhouse gases, which can increase up to 130% by 2050 at current rates.[1] Alternative energy sources must be developed to meet the projected energy demand in the future in a sustainable and environmentally conscious manner. Bio-oils generated via biomass fast pyrolysis represent an attractive avenue for the production of renewable fuels and chemicals. The key challenge in bio-oil upgrading is the development of a catalytic system that can efficiently deoxygenate various classes of compounds, particularly from the lignin-derived fraction, under mild reaction conditions. Lignin-derived phenolic compounds are much more refractory than other types of oxygenates found in biomass, requiring high H<sub>2</sub> pressures and catalysts containing precious metals for upgrading. In this contribution, we show that MoO<sub>3</sub> is a promising catalyst to selectively transform various phenolic compounds into aromatic hydrocarbons in high yields using low H<sub>2</sub> pressures by eliminating oxygen-containing functional groups without saturating the aromatic ring. The catalyst's original activity can be retrieved by simple calcination, thus showing that it is not only highly active and selective, but also robust.

### Introduction

The utilisation of lignocellulosic biomass as a source of renewable carbon for the production of fuels and chemicals has garnered much attention in the last decade. Among the various technologies investigated for lignocellulosic biomass processing, fast pyrolysis and catalytic fast pyrolysis have emerged as attractive and economically viable options.[3-5] Although the liquid products from these pyrolysis processes, (i.e., bio-oil) exhibit moderate energy densities, they cannot be directly utilised as transportation fuels without a prior upgrading step. Further upgrading is required because oxygen and water content of bio-oil is too high, resulting in several drawbacks that include low energy density, immiscibility with hydrocarbons, and wide variation in boiling point temperatures.[6,7] Moreover, bio-oil has high acid content, making it very reactive and unstable during transportation and storage. Bio-oil is considered a hydrogen-deficient feedstock, requiring the use of hydrogen for all upgrading processes. Hydrogen can be obtained from different sources, including steam reforming of methane abundant shale gas reserves,

catalytic reforming of biomass-derived feedstock, or, ideally, solar-based water splitting. [8]

Lignin-derived phenolic compounds represent a significant fraction of bio-oil. Lignin comprises up to 30 wt% of lignocellulosic biomass and it is composed of a heterogeneous, amorphous matrix of polyaromatic units featuring numerous ether linkages (C–O–C), as well as hydroxyl (–OH), and methoxyl (–OMe) side groups. Unfortunately, these phenolic molecules are much more refractory than sugar-derived oxygenates and their effective processing currently represents one of the grand-challenges in bio-oil upgrading.[9-11]

Hydrodeoxygenation (HDO) of biomass components involves direct removal of oxygen from bio-oil via C–O bond cleavage. HDO processes for phenolic compounds are challenging since high yields of aromatic hydrocarbons can only be achieved by selectively cleaving the strong C–O bond without hydrogenation the aromatic ring. Excellent reviews are available on HDO catalysts for lignin-derived molecules that highlight the main bottlenecks faced during processing.[12,13] Supported noble metals such as Ru, Rh, Pd, Pt, Re, as well as base metals, such as Cu, Ni, Fe and their heterometallic alloys are active for hydrogenation/hydrogenolysis reactions, but demand high H<sub>2</sub> pressures and high temperatures, which typically promote saturation of all double bonds.[14,15]. Molybdenumbased sulphides (such as MoS<sub>2</sub>, NiMoS<sub>2</sub>, and CoMoS<sub>2</sub>), the typical industrial hydrotreating catalysts in refining, are active HDO catalysts under high operating H<sub>2</sub> pressures (15–80 bar), but experience a rapid deactivation in the absence of a sulphur source and are sensitive to coke formation and water poisoning.[16-18] Metal phosphides, such as Ni<sub>2</sub>P, have shown higher HDO activity than commercial sulphide catalysts for the conversion of guaiacol into phenol and benzene.[19,20] Recently, Hicks and co-workers showed that a bimetallic FeMoP catalyst is active and selective for C–O bond cleavage of phenolics and aryl ethers in the liquid phase, producing benzene with selectivities exceeding 90% at 673 K, but require H<sub>2</sub> pressures in the range of 21–42 bar.[21] Bifunctional (metal/acid) catalysts consisting of noble metals supported on acid supports, such as Pt/H-Beta and Ga/H-Beta, generate aromatics (benzene, toluene and xylene) during vapour-phase processing of anisole and *m*-cresol feeds under atmospheric H<sub>2</sub> pressure at 673–823 K and in aqueous phase conditions under high H<sub>2</sub> pressures (>50 bar) but only in moderate yields.[22-33]

Many challenges remain for the development of HDO catalysts for bio-oil upgrading that do not use expensive noble metals, that utilise minimum amounts of H<sub>2</sub> (i.e., low H<sub>2</sub> pressures), and feature high stability. Recently, we demonstrated that MoO<sub>3</sub> is an attractive, earth-abundant catalyst active for the HDO of various biomass-derived oxygenates, including aliphatic and cyclic ketones, furanics, and phenolic feeds. Importantly, it was shown that MoO<sub>3</sub> selectively cleaves C–O bonds to produce olefinic and aromatic hydrocarbons, with high activity and selectivity using low H<sub>2</sub> pressures (≤1 bar).[34] We inferred that oxygen vacancies play an important role in the reaction mechanism, but the nature of the active site(s) was not identified. Chen and co-workers presented a similar catalytic behaviour on transition-metal carbide catalysts, for the conversion of C<sub>3</sub> oxygenates (e.g., propanal, propanol and acetone) into propylene under low H<sub>2</sub> pressures and temperatures between 573–653K.[35,36]

In this contribution, we report the high selectivity, stability, and hydrogen efficiency of MoO<sub>3</sub> catalysts to produce aromatic hydrocarbons from a set of lignin-derived model compounds

that represent the spectrum of C–O bonds present in real lignin fractions. Bond-dissociation energies (BDEs) of relevant C–O bonds involved in the HDO of these model compounds were estimated by density functional theory (DFT) computational methods. Next, catalyst performance, temperature effects, stability, and regenerability were investigated and compared with predicted reactivity trends from the BDE analysis. Finally, catalyst characterisation methods during the course of the HDO reaction were used to reveal the transition of the catalyst surface from an oxide phase to oxycarbide and oxycarbohydride phases. Systematic catalyst pretreatments were performed to gain understanding of the nature and genesis of surface active sites.

## Experimental section

### Chemicals and materials

Phenol (≥99 wt%), *m*-cresol (99 wt%), anisole (>99 wt%), guaiacol (≥98 wt%) and diphenyl ether (≥99 wt%) obtained from Sigma-Aldrich were used as feeds with no further purification. H<sub>2</sub> (99.999%, Airgas) and He (99.998%, Airgas) were used as a reactant in the reaction experiments, and as an inert carrier gas, respectively. O<sub>2</sub> (99.999%, Airgas) and air (zero grade, Airgas) were used for catalyst regeneration. *Isobutane* (Airgas) and zinc granules (-20 mesh, 99.8%, Alfa Aesar) were used during the synthesis of molybdenum oxycarbohydride. Commercial molybdenum(VI) oxide, MoO<sub>3</sub> (≥99.5 wt%), molybdenum(IV) oxide, MoO<sub>2</sub> (≥99 wt%), and molybdenum carbide, Mo<sub>2</sub>C (≥99.5 wt%) were purchased from Sigma-Aldrich. Prior to reaction, MoO<sub>3</sub> was calcined at 873 K (with a ramp rate of 10 K min<sup>-1</sup>) for 3 h under air flow (100 mL min<sup>-1</sup>).

A phase pure molybdenum oxycarbohydride (MoO<sub>x</sub>C<sub>y</sub>H<sub>z</sub>) sample was synthesised according to the procedure used by Glemser and Lutz.[37] Briefly, bulk commercial MoO<sub>3</sub> was added into a 4N HCl aqueous solution containing an excess amount of Zn granules. Evolved hydrogen generated *in-situ* intercalates between the layers of MoO<sub>3</sub> to form a hydrogen bronze. The resulting slurry was washed with a generous amount of deionised water to remove ZnCl<sub>2</sub> and remaining HCl. The absence of chlorine ion was detected by AgNO<sub>3</sub> test, and the excess Zn granules were sieved out. The hydrogen bronze of molybdenum oxide was treated with a flow of H<sub>2</sub>/*i*-butane (200 mL min<sup>-1</sup>, 3:1 v/v H<sub>2</sub>/*i*-butane mixture) at 623 K for 12 h to produce the oxycarbohydride.[38,39] The final product was dried under vacuum and stored under moisture- and oxygen-free conditions.

### Catalyst activity measurement

The catalytic testing experiments were conducted in a vapour-phase packed-bed flow reactor system. A stainless steel tube of 0.95 cm OD (wall thickness 0.089 cm) was used as the reactor, which was mounted in an insulated single-zone furnace (850W/115V, Applied Test Systems Series 3210). Temperature was controlled using a thermocouple mounted slightly downstream of the catalyst bed (Omega, model TJ36-CAXL-116u) connected to a temperature controller (Digi-Sense, model 68900-10). The MoO<sub>3</sub> catalyst bed (20–300 mg) was mixed with an inert ( $\alpha$ -alumina, Sigma-Aldrich) sieved through a 100–200 mesh. The bed volume was typically 2 mL and situated in the middle of the furnace. Liquid reactants were introduced into the reactor via a syringe pump (Harvard

Apparatus, model 703005). In the case of phenol feed, the solid reactant was mixed with an unreactive solvent, (e.g., 20 wt% in mesitylene), prior to loading into the syringe. Carrier He gas or reactant H<sub>2</sub> gas was mixed with vapourised reactants at the inlet of the reactor. Each experiment was carried out at 573–673 K and atmospheric pressure with a constant total gas flow rate of 70 mL min<sup>-1</sup>. All experiments were carried out under conditions free of mass transfer limitations.[34] The space-time (W/F), expressed in g<sub>Cat</sub> (mmol<sub>Feed</sub> h<sup>-1</sup>)<sup>-1</sup>, is defined as the ratio between the mass of the catalyst and the molar feed rate of the reactants. For catalyst regeneration experiments, spent catalysts were calcined *in situ* under pure O<sub>2</sub> or air at 593–673 K for 3 h.

### Product analysis and data evaluation

The reactor effluent lines were heated at 523 K to prevent any condensation of products, which were directly analysed and quantified by an online gas chromatographer equipped with a flame ionisation detector (GC-FID, Agilent Technologies, model 7890A) equipped with a DB-5 column (Agilent, 30 m × 0.25 mm id, 0.25 μm). The GC was operated with ultra-high purity helium as the carrier gas at a constant flow rate of 1.0 mL min<sup>-1</sup>. The GC parameters used for the analysis were as follows: injector temperature 523 K; detector temperature 573 K; split ratio 1:100. The temperature program started at 343 K and held for 5 minutes; then the temperature was increased at 20 K min<sup>-1</sup> to 533 K, followed by a 7-min hold. Product identification was performed using a mass selective detector (MSD, Agilent Technologies, model 5975C). The nature and quantity of carbon residues on spent catalysts were analysed by a combination of thermogravimetric analysis (TGA, TA Instruments TGA-Q500) and mass spectrometry (MS, Hiden Analytical HPR-20/QIC). The TGA-MS experiments were performed by using 5 vol% O<sub>2</sub>/He with a total flow rate of 100 mL min<sup>-1</sup>. The temperature was ramped from 323 K to 923 K with a heating rate of 7.5 K min<sup>-1</sup> and held at the final temperature for 30 min. The evolution of CO<sub>2</sub> (*m/z* = 44) and H<sub>2</sub>O (*m/z* = 18) were continuously monitored by the MS.

The following definitions are used to quantitate experimental data:

$$\text{Conversion\%} = \frac{\text{moles of carbon in reactant consumed}}{\text{moles of carbon in reactant fed}} \times 100 \quad (1)$$

$$\begin{aligned} \text{Selectivity to hydrocarbons\%} \\ = \frac{\text{sum of moles in aromatic products}}{\text{moles of carbon in reactant consumed}} \times 100 \end{aligned} \quad (2)$$

$$\text{Yield\%} = \frac{\text{sum of carbon in product}}{\text{moles of carbon in reactant fed}} \times 100 \quad (3)$$

The catalyst deactivation profiles were obtained using a first-order decay kinetic model.[40] The activity of the catalyst is given by:

$$a(t) = \frac{-r_A}{-r_{A(\text{fresh})}} = \frac{\text{rate of reaction A at any time } t}{\text{rate of reaction A with fresh catalyst}} \quad (4)$$

For first-order decay:

$$a(t) = \exp(-k_{\text{Deact}} t), \text{ where } a(t) = C \text{Ln}\left(\frac{1}{1-x}\right) \quad (5)$$

Combining gives:

$$\text{Ln Ln}\left(\frac{1}{1-x}\right) = -k_{\text{Deact}} t + C' \quad (6)$$

where *x* = fractional conversion, *k*<sub>Deact</sub> = first-order deactivation rate constant, and *t* = time.

### Characterisation

The powder X-ray diffraction (PXRD) patterns of fresh and spent catalyst samples were recorded on a Bruker D8 Discover diffractometer, equipped with a Nickel-filtered Cu-Kα radiation (λ = 1.5418 Å). Diffraction data recorded on a 2D image plate were integrated between 20° and 90° 2θ. The surface area was determined by nitrogen adsorption/desorption experiment using a Quantachrome Autosorb iQ automated gas sorption system. X-Ray photoelectron spectroscopy (XPS) data were collected using a PHI Versaprobe II equipped with a multichannel hemispherical analyser and aluminium anode X-ray source operating at 100 W with a 100-μm beam scanned over a 1.4-mm line across the sample surface. A dual-beam charge neutralisation system was used with an electron neutraliser bias of 1.2 eV and Argon ion beam energy of 10 eV.

### Computational methods

Lignin-derived model compounds and their corresponding radicals were fully optimised at the DFT/B3LYP/6-311+G(d,p) level of theory using Gaussian 09 software.[41,42-44] Frequency calculations were performed at the same level of the theory to characterise the stationary points and evaluate the energetics. The homolytic C–O bond-dissociation energies (BDEs) of the compounds were estimated from the expression:



where C<sub>x</sub>–O<sub>y</sub> = parent lignin-derived compounds; C<sub>x</sub><sup>•</sup> = phenyl, its derivative or methyl radicals; and O<sub>y</sub><sup>•</sup> = hydroxy, methoxy or phenolate radicals. The C–O BDEs were calculated as follows:

$$\text{BDE} = H(\text{C}_x^\bullet) + H(\text{O}_y^\bullet) - H(\text{C}_x\text{-O}_y) \quad (8)$$

where *H*(*i*)s are the enthalpies of different species *i*, at 593 K in the gas phase.

## Results and discussion

### C–O BDE analysis

The energetics of the different types of C–O bonds in lignin-derived model compounds were computed to gain insight into HDO processes. Three types of C–O bonds were considered: 1) the bond between C<sub>Aromatic</sub> and O<sub>Hydroxy</sub> (i.e., Ph–OH); 2) the bond between C<sub>Aromatic</sub> and O<sub>Methoxy</sub> (i.e., Ph–OMe); and 3) the etheric bonds between O<sub>Phenolate</sub> and C<sub>Methyl</sub> or C<sub>Aromatic</sub> (i.e., Ph–O–Me or Ph–O–Ph, respectively). The C–O BDEs of three monolignols featuring these types of bonds, namely *p*-coumaryl alcohol (Cou), coniferyl alcohol (Con) and sinapyl alcohol (Sin) were calculated to assess the effect of type, number, and position of the functional groups on the BDE. (see Fig. S1) The *p*-coumaryl alcohol, containing a cinnamyl alcohol unit with one –OH substituent, possesses one C–O bond with BDE(Ph–OH)<sub>Cou</sub> of 106.7 kcal mol<sup>-1</sup>. Coniferyl alcohol

contains three different C–O bonds with BDEs of 105.2 kcal mol<sup>-1</sup>, 90.7 kcal mol<sup>-1</sup>, and 54.2 kcal mol<sup>-1</sup> for (Ph–OH)<sub>Con</sub>, (Ph–OMe)<sub>Con</sub>, and (Ph–O–Me)<sub>Con</sub>, respectively. Sinapyl alcohol, contains one –OH and two –OMe substituents, with calculated BDEs of 108.4 kcal mol<sup>-1</sup>, 91.1±1.3 kcal mol<sup>-1</sup>, and 51.2±3.1 kcal mol<sup>-1</sup> for (Ph–OH)<sub>Sin</sub>, (Ph–OMe)<sub>Sin</sub>, and (Ph–O–Me)<sub>Sin</sub>, respectively. The calculations indicate that the BDEs of each type of C–O bond are not influenced significantly by the number or type of additional substituents, and follow an order of Ph–OH (106.8±1.6 kcal mol<sup>-1</sup>) > Ph–OMe (91.5±1.4 kcal mol<sup>-1</sup>) > Ph–O–Me (52.2±3.5 kcal mol<sup>-1</sup>). The estimated BDE numbers and trend are consistent with previously-reported experimental values.[45]

A similar BDE analysis was applied to the model compounds phenol, *m*-cresol, anisole, guaiacol, and diphenyl ether. The energetics of C–O bonds in the model compounds correlate well with those in the real lignin monomers and show a trend of Ph–OH > Ph–OMe > Ph–O–Ph > Ph–O–Me (see Fig. 1). Specifically, the BDEs of (Ph–OH) in phenol (106.1 kcal mol<sup>-1</sup>), *m*-cresol (106.0 kcal mol<sup>-1</sup>) and guaiacol (109.2 kcal mol<sup>-1</sup>) are similar to the average (Ph–OH) BDEs in the monolignols (106.8±1.6 kcal mol<sup>-1</sup>). Similarly, comparable values were obtained for the (Ph–OMe) and (Ph–O–Me) bonds of anisole and guaiacol when compared to the analogous groups in sinapyl alcohol. The BDE for diphenyl ether, BDE(Ph–O–Ph) was 69.7 kcal mol<sup>-1</sup>, which lies in between the BDEs for (Ph–OMe) and BDEs(Ph–O–Me). As expected, the BDE analysis shows that an etheric C–O bond (i.e., Ph–O–Ph and Ph–O–Me) is weaker than a phenolic C–O bond (e.g., Ph–OH and Ph–OMe).

### Conversion of lignin-derived model compounds

Table 1 shows the total conversion and the corresponding product distribution from reacting lignin-derived model compounds with MoO<sub>3</sub> under atmospheric pressure at 593 K and identical contact time (W/F, defined as g<sub>Cat</sub> (mmol<sub>Feed</sub> h<sup>-1</sup>)<sup>-1</sup>). Prior to each run, the catalyst was treated under flowing H<sub>2</sub> at 593 K for 3 h. Phenol was converted to benzene with a selectivity of 94% at 29% conversion. Neither cyclohexane nor cyclohexene was observed in the product mixture, thus indicating that deoxygenation via ring saturation followed by dehydration is unlikely and instead suggests a pathway involving direct C–O bond cleavage. Similarly *m*-cresol was converted to toluene with 99% selectivity at 49% conversion. At 79% conversion, anisole yielded 44% benzene and 20% alkylbenzenes. Minor phenolic products included phenol, methyl anisole, cresol, and alkylphenols with yields of 2%, 1%, 3%, and 3%, respectively. In a similar manner, benzene, alkylbenzenes, phenol, and alkylated phenols were mainly produced from guaiacol with yields of 12%, 9%, 31% and 9%, respectively, while methane (6% yield) and methanol (2% yield) were also detected as minor products. Diphenyl ether was selectively converted to benzene with 87% selectivity at 83% conversion. Overall carbon balances typically exceeded 94%, with the remaining carbon being assigned to soft coke and carbon intercalation into the oxide lattice, as analysed by TGA–MS and XRD of the spent catalysts (vide infra).

These reactivity data suggest that MoO<sub>3</sub> promotes both deoxygenation and demethylation/transalkylation reactions in the presence of methoxy substituents in the ring. To identify primary products, the HDO of anisole was investigated under differential conditions. As shown in Table 2, the ratio of total aromatic hydrocarbons to total phenolic intermediates is

approximately 1:1 when extrapolated to 0% conversion. Consequently, the selectivity to aromatic hydrocarbons continues to increase with increasing conversion once the phenolic intermediates also undergo HDO reactions. These results indicate that the strength of the relevant C–O bonds in the feed molecules cannot always explain observed product distributions. Thus, it is expected that the weaker etheric C–O bonds of an aryl ether (e.g., Ph–O–Ph bond of diphenyl ether) or a methoxy group (e.g., Ph–O–Me bond of anisole or guaiacol) would be more reactive than the C<sub>Aromatic</sub>–O bonds (e.g., Ph–OH bond of phenol or guaiacol, and Ph–OMe bond of anisole or guaiacol). However, while diphenyl ether showed the highest level of conversion amongst the model compounds investigated, the model compounds containing, methoxy groups, such as anisole and guaiacol, showed that demethylation/transmethylation reactions resulting from cleaving weaker aliphatic C–O bonds to yield phenolic products and methane do not dominate over phenolic Ph–OMe bond cleavage to produce benzene, methanol, and other transalkylated aromatic hydrocarbons directly. As expected, the yield of aromatics increases with increasing conversion (see Table 2). Specifically, the selectivity toward aromatic hydrocarbons increased from 40 to 82% when the conversion increased from 6 to 79%. Note that MoO<sub>3</sub> effectively minimises carbon loss in the final product by promoting transmethylation reactions of the methanol byproduct and/or the anisole feed itself with the aromatic ring to form alkylbenzenes.

### Catalyst stability

Fig. 2 shows the results of investigating catalyst stability over a temperature range of 573 K to 673 K using *m*-cresol as feed. The MoO<sub>3</sub> catalyst bed was treated under flowing He during the temperature ramp, and once the target temperature was reached, the feed/H<sub>2</sub> mixture was introduced. At the highest reaction temperature (i.e., 673 K), complete *m*-cresol conversion was observed at short time-on-stream (TOS). However, rapid deactivation ensued to reach ca. 10% conversion after 4 h, followed by a slower deactivation rate from 4 to 7 h TOS. (see Fig. 2a). A first-order deactivation model accurately captures the deactivation profile, generating *k*<sub>Deact</sub> of 0.898 h<sup>-1</sup> and 0.156 h<sup>-1</sup> for the 0–4 h and 4–7 h regimes, respectively. This catalytic behaviour is consistent with results obtained previously with MoO<sub>3</sub> during acetone HDO under similar reaction conditions.[34] At a lower reaction temperature (i.e., ≤ 623 K), the catalyst showed drastically slower deactivation kinetics. Specifically, at temperatures below 623 K, a single deactivation regime exists in the 24 h period investigated (see Figs. S2) and first-order deactivation constants of 0.149 h<sup>-1</sup>, 0.058 h<sup>-1</sup>, 0.048 h<sup>-1</sup> were obtained for data collected at 623, 593 and 573 K, respectively (see Fig. 2b). These values translate to deactivation rates that are ~6, ~15, and ~19 times slower than the deactivation rate observed at 673 K. Interestingly, an induction period was observed wherein the catalyst requires ca. 1 h to display full catalytic activity. We hypothesise that the catalyst surface undergoes an *in-situ* modification during the induction period which promotes both increased activity and stability. An optimal temperature of 593 K was used for all further HDO studies.

### Spent catalyst analysis

To gain a better understanding of the deactivation mechanism and the observed induction period, the spent

catalysts were characterised using PXRD, TGA-MS, and XPS. PXRD patterns in Fig. 3 indicate that  $\text{MoO}_3$  undergoes drastic phase transformations regardless of the reaction temperature used. Specifically, analysis of the spent catalyst used at 673 K shows that  $\text{MoO}_3$  reduces into a catalytically-inactive  $\text{MoO}_2$  phase, which is consistent with the observed fast deactivation at this temperature (see Fig 3d). Ressler and co-workers used *in situ* XRD and XAFS techniques to show the transformation of  $\text{MoO}_3$  into  $\text{MoO}_2$  at temperatures above 623 K.[46] At temperatures below 623 K, a mixed phase consisting primarily of  $\text{MoO}_x\text{C}_y\text{H}_z$  with minor  $\text{MoO}_2$  impurities was identified. The identity of the oxycarbohydride was confirmed by comparing PXRD patterns of the spent catalyst with a phase pure  $\text{MoO}_x\text{C}_y\text{H}_z$  synthesised using the protocols outlined by Ledoux and co-workers (see Fig 3e-g). [38,39]

Temperature-programmed oxidation (TPO) studies of the spent catalysts were carried out to gain insights into the nature of the carbonaceous species present post-reaction (see Fig. 4). Reference materials, including activated carbon, “soft coke”,  $\text{Mo}_2\text{C}$  and  $\text{MoO}_x\text{C}_y\text{H}_z$ , were used to establish 3 different  $\text{CO}_2$ -evolution temperature zones. The low temperature zone 1 (550–630 K) was based on the TPO of  $\text{Mo}_2\text{C}$  (spectrum h, Fig. 4), while the high temperature zone 3 (above 750K) was based on the TPO of graphitic carbon (spectrum a, Fig. 4). The intermediate temperature zone 2 (630–750K) was based on the TPO of both  $\text{MoO}_x\text{C}_y\text{H}_z$  (spectrum f, Fig. 4) and the “soft coke” sample prepared by treating the  $\text{MoO}_3$  with *m*-cresol feed under  $\text{He}$  at 593 K for 3 h (spectrum g, Fig. 4). The “soft coke” sample is intended to represent the carbonaceous residue present after the reaction. The oxidation of a molybdenum oxycarbohydride ( $\text{MoO}_x\text{C}_y\text{H}_z$ ) has been previously shown to occur at temperatures between 668–693 K.[38,39,47] For all spent catalysts,  $\text{CO}_2$  and  $\text{H}_2\text{O}$  evolution were detected within zone 2, suggesting that the carbonaceous species are likely a combination of oxycarbide carbon and soft coke (see Fig. S3).

TGA data confirm that the overall carbon contents on the spent catalysts at 573, 593, 623 and 673 K are 3.7, 4.6, 6.5 and 7.1 wt%, respectively. It is noted that the amount of carbon from the 673 K run is comparable to those from lower temperature runs; however, only contributions from soft coke are expected for this sample since the  $\text{MoO}_x\text{C}_y\text{H}_z$  phase was not detected by PXRD (spectrum d, Fig. 3). The TPO profiles show that calcining under pure  $\text{O}_2$  flow at 673 K should regenerate the spent catalysts. A regeneration study confirmed that catalytic activity and selectivity can be completely recovered when calcining the catalyst at 673 K for 3 h (see Fig. 5). The use of either pure  $\text{O}_2$  or air at a lower calcination temperature (i.e., 623 K) is insufficient to regenerate the  $\text{MoO}_3$  catalyst. (see Fig. S4) Although it has been shown that  $\text{MoO}_2$  can be fully oxidised to  $\text{MoO}_3$  at 623 K,[48] this temperature is too low to burn off the deposited soft coke on the catalyst surface as evidenced by the lack of  $\text{CO}_2$  evolution during TPO at temperatures below 623 K.

### Induction period and carburisation of $\text{MoO}_3$

A systematic investigation of different pretreatment conditions on the  $\text{MoO}_3$  catalyst was performed to gain insight into the effect of the pre-reduction and surface carbon incorporation on catalyst activity. Fig. 6 shows the impact of the  $\text{H}_2$  pre-reduction (593 K and atmospheric pressure) on the initial HDO activity of *m*-cresol conversion at 593 K. Exposing the  $\text{MoO}_3$  catalyst to a  $\text{H}_2$  flow for 3 h prior to the  $\text{H}_2$ /feed mixture completely eliminated the induction period, generating the

maximum steady-state conversion (~50%) observed for the non-pretreated catalyst from the beginning of the experiment. The catalyst deactivation profile remained virtually identical after reaching steady state (see Fig. 6b). PXRD patterns revealed that  $\text{MoO}_3$  does not undergo a phase transformation after  $\text{H}_2$  reduction at 593 K up to 3.5 h (see spectra b and c, Fig. 7). However, after a 7 h reduction,  $\text{MoO}_3$  is transformed mostly into  $\text{MoO}_2$  with trace amounts of an oxyhydride ( $\text{MoO}_x\text{H}_z$ ) phase (see spectrum d, Fig. 7).[49,50] In the absence of  $\text{H}_2$ , treating  $\text{MoO}_3$  with *m*-cresol under  $\text{He}$  for 3 h did not result in the formation of an oxycarbide phase (see spectrum e, Fig. 7). Interestingly, when pre-reduced  $\text{MoO}_3$  ( $\text{H}_2$  for 3 h at 593 K) is exposed to an *m*-cresol feed for 0.5 h, a  $\text{MoO}_x\text{C}_y\text{H}_z$  phase is observed along with  $\text{MoO}_2$  (see spectrum f, Fig. 7). Similar mixed phases of  $\text{MoO}_x\text{C}_y\text{H}_z$  and  $\text{MoO}_2$  are also observed when a  $\text{MoO}_3$  sample is treated with a *m*-cresol/ $\text{H}_2$  mixture for 3.5 h at 593 K (compare spectra f and g, Fig. 7); however, exposing  $\text{MoO}_3$  to an *m*-cresol/ $\text{H}_2$  mixture for 0.5 h is insufficient to create the oxycarbohydride phase (compare spectra g and h, Fig. 7). Unlike the synthesis of a pure  $\text{MoO}_x\text{C}_y\text{H}_z$  phase from the bronze precursor, the concomitant formation of  $\text{MoO}_2$  phase is inevitable when bulk  $\text{MoO}_3$  is used as a starting material.[51] These results indicate that the  $\text{H}_2$  pre-reduction is essential to activate the  $\text{MoO}_3$  surface, and the oxycarbohydride phase can be readily formed upon the introduction of a carbon source (i.e., *m*-cresol). In agreement with the observations by Ledoux and co-workers, we posit that during the  $\text{H}_2$  reduction, the  $\text{MoO}_3$  structure undergoes a shared-plan reconstruction, wherein freshly-created oxygen vacancies are quickly filled with carbon to create an oxycarbohydride phase that slows down the formation of unreactive  $\text{MoO}_2$ .[50]

The  $\text{MoO}_x\text{C}_y\text{H}_z$  phase is created from an *in-situ* surface modification of  $\text{MoO}_3$  during reaction. To investigate the dynamics of this transition, we performed PXRD analysis on samples extracted from the reactor at different times on stream for reactions performed at two different temperatures (see Fig. 8). At 673 K, the starting  $\text{MoO}_3$  catalyst is fully converted into  $\text{MoO}_2$  after 0.5 h. The catalyst undergoes severe deactivation, losing over 80% of its activity by 3 h. At 593 K, a drastically different behaviour is observed. After 0.5 h,  $\text{MoO}_3$  does not undergo a phase transformation and HDO activity is clearly located within the induction period regime. After 1.5 h, the  $\text{MoO}_3$  is completely transformed into an oxycarbohydride ( $\text{MoO}_x\text{C}_y\text{H}_z$ ) phase containing  $\text{MoO}_2$  impurities and reactivity is located at the steady-state regime. This phase is maintained throughout the entire experiment with the catalyst undergoing a slight first-order deactivation. When comparing both analyses, the experimental data indicates that below 623 K, the catalyst features improved stability and selectivity when the  $\text{MoO}_x\text{C}_y\text{H}_z$  phase is present.

Recently, it has been reported that  $\text{Mo}_2\text{C}$  and WC are active for HDO of small oxygenates and selective toward olefin productions.[35,36] The materials were synthesised, and tested in a vapour-phase under low  $\text{H}_2$  pressure at 573–653K. However, no characterisation data was provided to show if an oxycarbide phase was present. It is possible that  $\text{Mo}_2\text{C}$  may undergo partial oxidation to form an oxycarbide during the reaction.[52,53] Weckhuysen and co-workers tested  $\text{Mo}_2\text{C}$  and  $\text{W}_2\text{C}$  supported on carbon-nanofibers for the HDO of guaiacol in liquid phase and 55 bar  $\text{H}_2$  pressure at 573–648 K, but observed mainly phenol and cresols with concomitant poor hydrocarbon yields (<10%).[54] Unfortunately, the nature of catalytic sites on the carbide catalysts remains unidentified.

A  $\text{MoO}_x\text{C}_y\text{H}_z$  phase has been suggested as the active phase, for the isomerisation of *n*-alkanes to *i*-alkanes.[39,49,50] The reaction proceeds via a bond-shift mechanism involving metallocyclic intermediates. Other reports suggest that a molybdenum suboxide ( $\text{MoO}_{3-x}$ ) is responsible for the active site, and the reaction proceeds via a conventional bifunctional pathway.[55-59] Goguet and co-workers observed the formation of an oxycarbide phase on the  $\text{MoO}_3$  catalyst, but indicated that lattice carbon did not influence isomerisation activity.[60] Nonetheless, both phases (i.e.,  $\text{MoO}_x\text{C}_y\text{H}_z$  or  $\text{MoO}_{3-x}$ ) contain lower valence  $\text{Mo}^{5+}$  and  $\text{Mo}^{4+}$  states.[50,56] Control experiments show that  $\text{MoO}_2$  and  $\text{MoS}_2$  (i.e.,  $\text{Mo}^{4+}$  state) are completely inactive for the HDO of phenolic compounds. Since pristine  $\text{MoO}_3$  (i.e.,  $\text{Mo}^{6+}$  state) shows an induction period when treated with a  $\text{H}_2$ /carbon mixture, we hypothesise that  $\text{Mo}^{5+}$  species are required to promote HDO chemistry.  $\text{Mo}^{5+}$  species can be generated either from the carburisation of  $\text{MoO}_3$  to  $\text{MoO}_x\text{C}_y\text{H}_z$  or during the reduction of  $\text{MoO}_3$  to  $\text{MoO}_{3-x}$  in the presence of  $\text{H}_2$ . Our data does not allow us to discriminate species between these two scenarios for the creation of  $\text{Mo}^{5+}$  species. However, lattice carbon may help in the stabilisation of the  $\text{Mo}^{5+}$  state, preventing over-reduction of  $\text{Mo}^{6+}$  to  $\text{Mo}^{4+}$  by creating an oxycarbide phase. Fig. 9 presents the surface characterisation of the spent catalysts by the XPS. The Mo 3d doublet contains mixed oxidation states with contributions from  $\text{Mo}^{4+}$ ,  $\text{Mo}^{5+}$ , and  $\text{Mo}^{6+}$  with the  $3d_{5/2}$  bands located at 229.7, 230.8 and 232.6 eV, respectively.[50,56] No signals corresponding to  $\text{Mo}_2\text{C}$  (i.e.,  $\text{Mo}^{2+}$  state) or Mo metal (i.e.,  $\text{Mo}^0$  state) were detected. Signals associated with surface  $\text{Mo}^{6+}$  were generated during  $\text{O}_2$  passivation. Peak integration shows that the  $\text{MoO}_2$  sample contains only 13% of  $\text{Mo}^{5+}$  thus confirming that its formation from  $\text{Mo}^{4+}$ , if possible, is fairly small (see Fig. S5). Therefore, the large amounts of the  $\text{Mo}^{5+}$  detected on the spent catalysts are derived from the *in-situ* surface modification of  $\text{MoO}_3$  by the  $\text{H}_2$ /feed mixture during reaction. The amount of  $\text{Mo}^{4+}$  increases with increasing reaction temperatures, which is consistent with a more severe reduction of  $\text{Mo}^{6+}$ . In contrast,  $\text{Mo}^{5+}$  is more prevalent at lower reaction temperatures, suggesting a more favourable formation of the oxycarbide. The XPS data is consistent with the PXRD patterns showing a more dominant  $\text{MoO}_2$  phase at a higher reaction temperature and a more dominant  $\text{MoO}_x\text{C}_y\text{H}_z$  phase at a lower one (see Fig. 3). The partially reduced  $\text{MoO}_3$  phase (i.e., presumably  $\text{Mo}^{5+}$  state) is expected to behave as a Lewis acid site (i.e., oxygen vacancy) that may weaken C–O bond upon adsorption of the molecule on the active site. Detailed computational studies on the reaction pathways on partially reduced surfaces of  $\text{MoO}_3$  are currently underway.

## Conclusion

$\text{MoO}_3$  is an effective catalyst for the HDO of various lignin-derived model compounds, including phenol, *m*-cresol, anisole, guaiacol, and diphenyl ether. The catalyst is capable of selectively converting all model compounds into aromatic hydrocarbons with high yields under atmospheric  $\text{H}_2$  pressures. The bond-dissociation energy (BDE) calculation suggests that the strength of each C–O bond type is only slightly influenced by number or type of additional substituents in the ring. The trend of BDEs follow an order of  $\text{Ph-OH} > \text{Ph-OMe} > \text{Ph-O-Ph} > \text{Ph-O-Me}$ , indicating an etheric C–O bond is generally more reactive than a  $\text{C}_{\text{Aromatic}}\text{-O}$  bond. Although diphenyl ether shows the highest reactivity of all model compounds tested,  $\text{MoO}_3$  preferentially cleaves phenolic

Ph–OMe over the weaker aliphatic Ph–O–Me bond. The catalyst undergoes first order deactivation at temperatures below 623 K, and the original HDO activity can be regained by a simple calcination of spent catalysts. During reaction, the catalyst undergoes a partial surface carburisation, which plays a role in stabilizing a  $\text{Mo}^{5+}$  state on the  $\text{MoO}_3$  surface and in slowing down the over reduction of  $\text{MoO}_3$  into an inactive  $\text{MoO}_2$  phase.

## Acknowledgements

This research was funded by British Petroleum (BP) through the MIT Energy Initiative Advanced Conversion Research Program. Generous allocations of computing time were provided by the OU Supercomputing Center for Education and Research (OSKER) at the University of Oklahoma. The authors would like to thank Sean T. Hunt for the acquiring the XPS spectra.

- 1 International Energy Agency, *Energy Technology Perspectives 2008*. IEA Publications, Paris, 2008.
- 2 U.S. Energy Information Administration, *International Energy Outlook 2013*, Report Number: DOE/EIA-0484 (2013)
- 3 E. Antonakou, A. Lappas, M. H. Nilsen, A. Bouzga and M. Stocker, *Fuel*, 2006, **85**, 2202–2212.
- 4 G. W. Huber and A. Corma, *Angew. Chem. Int. Ed.*, 2007, **46**, 7184–7201.
- 5 G. W. Huber, S. Iborra and A. Corma, *Chem. Rev.*, 2006, **106**, 4044–4098.
- 6 B. Scholze and D. Meier, *J. Anal. Appl. Pyrolysis*, 2001, **60**, 41–54.
- 7 A. Oasmaa and S. Czernik, *Energy Fuels*, 1999, **13**, 914–921.
- 8 R. D. Cortright, R. R. Davda, R. R. and J. A. Dumesic, *Nature*, 2002, **418**, 964–967.
- 9 Z. Y. Luo, S. R. Wang, Y. F. Liao, J. Zhou, Y. Gu and K. Cen, *Biomass Bioenergy*, 2004, **26**, 455–462.
- 10 A. G. Gayubo, A. T. Aguayo, A. Atutxa, R. Aguado and J. Bilbao, *Ind. Eng. Chem. Res.*, 2004, **43**, 2610–2618.
- 11 A. G. Gayubo, A. T. Aguayo, A. Atutxa, R. Aguado, M. Olazar and J. Bilbao, *Ind. Eng. Chem. Res.*, 2004, **43**, 2619–2624.
- 12 M. Saidi, F. Samimi, D. Karimipourfard, T. Nimmanwudipong, B. C. Gates and M. R. Rahimpour, *Energy Environ. Sci.*, 2014, **7**, 103–129.
- 13 H. Wang, J. Male and Y. Wang, *ACS Catal.*, 2013, **3**, 1047–1070.
- 14 C. R. Lee, J. S. Yoon, Y.-W. Suh, J.-W. Choi, J.-M. Ha, D. J. Suh and Y.-K. Park, *Catal. Commun.*, 2012, **17**, 54–58.
- 15 M. V. Bykova, D. Y. Ermakov, V. V. Kaichev, O. A. ulavchenko, A. A. Saraev, M. Y. Lebedev and V. A. Yafkovlev, *Appl. Catal. B*, 2012, **113–114**, 296–307.
- 16 M. Badawi, J. F. Paul, S. Cristol, E. Payen, Y. Romero, F. Richard, S. Brunet, D. Lambert, X. Portier, A. Popov, E.

- Kondratieva, J. M. Goupil, J. El Fallah, J. P. Gilson, L. Mariey, A. Travert and F. Maugé, *J. Catal.*, 2011, **282**, 155–164.
- 17 E. Laurent and B. Delmon, *J. Catal.*, 1994, **146**, 281–291.
- 18 O. İ. Şenol, T.-R. Viljava and A. O. I. Krause, *Catal. Today*, 2005, **106**, 186–189.
- 19 H. Y. Zhao, D. Li, P. Bui and S. T. Oyama, *Appl. Catal. A*, 2011, **391**, 305–310.
- 20 S.-K. Wu, P.-C. Lai, Y.-C. Lin, H.-P. Wan, H.-T. Lee and Y.-H. Chang, *ACS Sustainable Chem. Eng.*, 2013, **1**, 349–358.
- 21 D. J. Rensel, S. Rouvimov, M. E. Gina and J. C. Hicks, *J. Catal.*, 2013, **305**, 256–263.
- 22 X. Zhu, R. G. Mallison and D. E. Resasco, *Appl. Catal. A*, 2010, **379**, 172–181.
- 23 T. Prasomsri, A. T. To, S. Crossley, W. E. Alvarez and D. E. Resasco, *Appl. Catal. B*, 2011, **106**, 204–211.
- 24 T. Nimmanwudipong, R. C. Runnebaum, D. E. Block and B. C. Gates, *Energy Fuels*, 2011, **25**, 3417–3427.
- 25 T. Nimmanwudipong, R. C. Runnebaum, D. E. Block and B. C. Gates, *Catal. Lett.*, 2011, **141**, 1072–1078.
- 26 X. Zhu, L. L. Lobban, R. G. Mallinson and D. E. Resasco, *J. Catal.*, 2011, **281**, 21–29.
- 27 A. Ausavasukhi, Y. Huang, A. T. To, T. Sooknoi and D. E. Resasco, *J. Catal.*, 2012, **290**, 90–100.
- 28 C. Zhao, J. He, A. A. Lemonidou, X. B. Li and J. A. Lercher, *J. Catal.* 2011, **280**, 8–16.
- 29 C. Zhao and J. A. Lercher, *ChemCatChem*, 2012, **4**, 64–68.
- 30 C. Zhao and J. A. Lercher, *Angew. Chem. Int. Ed.*, 2012, **51**, 5935–5940.
- 31 C. Zhao, Y. Kou, A. A. Lemonidou, X. B. Li and J. A. Lercher, *Angew. Chem. Int. Ed.*, 2009, **48**, 3987–3990.
- 32 C. Zhao, Y. Kou, A. A. Lemonidou, X. B. Li and J. A. Lercher, *Chem. Commun.*, 2010, **46**, 412–414.
- 33 C. Zhao, D. M. Camaioni and J. A. Lercher, *J. Catal.* 2012, **288**, 92–103.
- 34 T. Prasomsri, T. Nimmanwudipong and Y. Román-Leshkov, *Energy Environ. Sci.*, 2013, **6**, 1732–1738.
- 35 H. Ren, W. Yu, M. Saliccioli, Y. Chen, Y. Huang, K. Xiong, D. G. Vlachos and J. G. Chen, *ChemSusChem*, 2013, **6**, 798–801.
- 36 H. Ren, Y. Chen, Y. Huang, W. Deng, D. G. Vlachos and J. G. Chen, *Green Chem.*, 2014, DOI: 10.1039/c3gc41256c
- 37 O. Glemser and G. Lutz, *Z. Anorg. Allg. Chem.*, 1951, **264**, 17–33.
- 38 C. Bouchy, C. Pham-Huu, B. Heinrich, E. G. Derouane, S. B. Derouane-Abd Hamid and M. J. Ledoux, *Appl. Catal. A*, 2001, **215**, 175–184.
- 39 C. Bouchy, C. Pham-Huu, B. Heinrich, C. Chaumont and M. J. Ledoux, *J. Catal.*, 2000, **190**, 92–103.
- 40 H. S. Fogler, “*Elements of Chemical Reaction Engineering*”. Prentice-Hall International Editions, 1987.
- 41 M. J. Frisch, G. W. Trucks, H. B. Schlegel, G. E. Scuseria, M. A. Robb, J. R. Cheeseman, G. Scalmani, V. Barone, B. Mennucci, G. A. Petersson, H. Nakatsuji, M. Caricato, X. Li, H. P. Hratchian, A. F. Izmaylov, J. Bloino, G. Zheng, J. L. Sonnenberg, M. Hada, M. Ehara, K. Toyota, R. Fukuda, J. Hasegawa, M. Ishida, T. Nakajima, Y. Honda, O. Kitao, H. Nakai, T. Vreven, J. A. Montgomery, Jr., J. E. Peralta, F. Ogliaro, M. Bearpark, J. J. Heyd, E. Brothers, K. N. Kudin, V. N. Staroverov, R. Kobayashi, J. Normand, K. Raghavachari, A. Rendell, J. C. Burant, S. S. Iyengar, J. Tomasi, M. Cossi, N. Rega, J. M. Millam, M. Klene, J. E. Knox, J. B. Cross, V. Bakken, C. Adamo, J. Jaramillo, R. Gomperts, R. E. Stratmann, O. Yazyev, A. J. Austin, R. Cammi, C. Pomelli, J. W. Ochterski, R. L. Martin, K. Morokuma, V. G. Zakrzewski, G. A. Voth, P. Salvador, J. J. Dannenberg, S. Dapprich, A. D. Daniels, Ö. Farkas, J. B. Foresman, J. V. Ortiz, J. Cioslowski, and D. J. Fox, Gaussian 09, Revision B.01, Gaussian, Inc., Wallingford CT, 2009.
- 42 A. D. Becke, *Phys. Rev. A*, 1988, **38**, 3098–3100.
- 43 C. Lee, W. Yang and R. G. Parr, *Phys. Rev. B*, 1988, **37**, 785–789.
- 44 A. D. Becke, *J. Chem. Phys.*, 1993, **98**, 5648–5652.
- 45 Y.-R. Luo, “*Handbook of bond dissociation energies in organic compounds*”. CRC Press LLC, 2003.
- 46 T. Ressler, R. E. Jentoft, J. Wienold, M. M. Günter and O. Timpe, *J. Phys. Chem. B*, 2000, **104**, 6360–6370.
- 47 G. Rodríguez-Gattorno, A. Martínez-Hernández, L. O. Aleman-Vizquez and E. Torres-García, *Appl. Catal. A*, 2003, **321**, 117–124.
- 48 T. Ressler, J. Wienold, R. E. Jentoft and T. Neisius, *J. Catal.*, 2002, **210**, 67–83.
- 49 C. Bouchy, C. Pham-huu and M. J. Ledoux, *J. Mol. Catal. A: Chem.*, 2000, **162**, 317–334.
- 50 P. Delporte, F. Meunier, C. Pham-Huu, P. Vennegues, M. J. Ledoux and Jean Guille, *Catal. Today*, 1995, **23**, 251–267.
- 51 P. Delporte, C. Pham-Huu and M. J. Ledoux, *Appl. Catal. A*, 1997, **149**, 151–180.
- 52 E. A. Blekkan, C. Pham-Huu, M. J. Ledoux and J. Guille, *Ind. Eng. Chem. Res.*, 1994, **33**, 1657–1664.
- 53 A. P. E. York, C. Pham-Huu, P. Del Gallo, E. A. Blekkan and M. J. Ledoux, *Ind. Eng. Chem. Res.*, 1996, **35**, 672–682.
- 54 A. L. Jongorius, R. W. Gosselink, J. Dijkstra, J. H. Bitter, P. C. A. Bruijninx and B. M. Weckhuysen, *ChemCatChem*, 2013, **5**, 2964–2972.
- 55 A. Benadda, A. Katrib and A. Barama, *Appl. Catal. A*, 2003, **251**, 93–105.
- 56 A. Katrib, A. Benadda, J. W. Sobczak and G. Maire, *Appl. Catal. A*, 2003, **242**, 31–40.
- 57 H. Sakagami, Y. Asano, N. Takahashi and T. Matsuda, *Appl. Catal. A*, 2005, **284**, 123–130.
- 58 T. Matsuda, H. Kodama, H. Sakagami and N. Takahashi, *Appl. Catal. A*, 2003, **248**, 269–278.

- 59 T. Matsuda, K. Watanabe, H. Sakagami and N. Takahashi, *Appl. Catal. A*, 2003, **242**, 267–274.
- 60 A. Goguet, S. Shekhtman, F. Cavallaro, C. Hardacre and F. C. Meunier, *Appl. Catal. A*, 2008, **344**, 30–35.

**Table 1** Conversion and product distribution of lignin-derived model compounds on MoO<sub>3</sub> catalysts<sup>a</sup>

Feed	Ph	Cr	An	Gua	DPE	
Temperature (K)	593	593	593	593	623	593
Conversion (C-mol%)	28.7	48.9	78.7	74.2	97.5	82.6
Selectivity to HCs	93.7	99.4	85.4	36.3	53.5	86.9
Yield (C-mol %)						
<i>Hydrocarbons</i>						
Methane	0	0	2.9	6.1	7.6	0
Benzene	26.9	0	44.0	11.9	32.8	71.8
Toluene	0	48.6	15.6	5.9	9.4	0
Other alkylbenzenes	0	0	4.7	3.0	2.4	0
<i>Oxygenates</i>						
Methanol	0	0	0.3	2.0	0.5	0
Anisole	0	0	21.3	2.3	10.8	0
Methyl anisole	0	0	1.3	0	0	0
Phenol	71.3	0	1.9	31.1	29.3	8.7
Cresol	0	51.1	2.9	6.6	0	0
Other alkylphenols	0	0	2.8	0	0	0
Guaiacol	0	0	0	25.8	2.5	0
Diphenyl ether	0	0	0	0	0	17.4
<b>Total carbon yield</b>	<b>98.2</b>	<b>99.7</b>	<b>97.5</b>	<b>94.8</b>	<b>95.3</b>	<b>98.0</b>

<sup>a</sup> Feed legend: phenol (Ph), *m*-cresol (Cr), anisole (An), guaiacol (Gua), and diphenyl ether (DPE). Reaction conditions:  $P_{\text{Total}} = 1.013$  bar (0.015 bar  $P_{\text{Feed}}$ , balance H<sub>2</sub>), W/F = 0.035 g<sub>Cat</sub> (mmol<sub>Feed</sub> h<sup>-1</sup>)<sup>-1</sup>, H<sub>2</sub> pre-reduction = 3 h, and TOS = 0.5 h.

**Table 2** Conversion and product distribution of anisole on MoO<sub>3</sub> catalysts at various W/F

W/F (g <sub>Cat</sub> (mmol <sub>Feed</sub> h <sup>-1</sup> ) <sup>-1</sup> )	0.0029	0.0078	0.035
Conversion (C-mol%)	6.0	22.9	78.7
Yield (C-mol %)			
<i>Hydrocarbons</i>			
Methane	0.2	1.7	2.9
Benzene	1.9	10.6	44.0
Toluene	0.4	1.3	15.6
Other alkylbenzenes	0.1	0.3	4.7
<i>Oxygenates</i>			
Methanol	0.1	0.2	0.3
Anisole	94.0	77.1	21.3
Methyl anisole	0.3	1.0	1.3
Phenol	1.1	2.7	1.9
Cresol	0.6	1.8	2.9
Other alkylphenols	0.3	1.0	2.8
<b>Total carbon yield</b>	<b>98.9</b>	<b>97.7</b>	<b>97.5</b>
Selectivity (C-mol %)			
Aromatic hydrocarbons	40.0	53.3	81.7
Phenolic products	38.3	28.4	11.3

Reaction conditions: Feed = anisole, T = 593 K,  $P_{\text{Total}} = 1.013$  bar (0.015 bar  $P_{\text{Feed}}$ , balance H<sub>2</sub>), pre-reduction = 3 h, and TOS = 0.5 h. Aromatic hydrocarbons = benzene + toluene + alkylbenzenes. Phenolic products = phenol + cresol + alkylphenols.

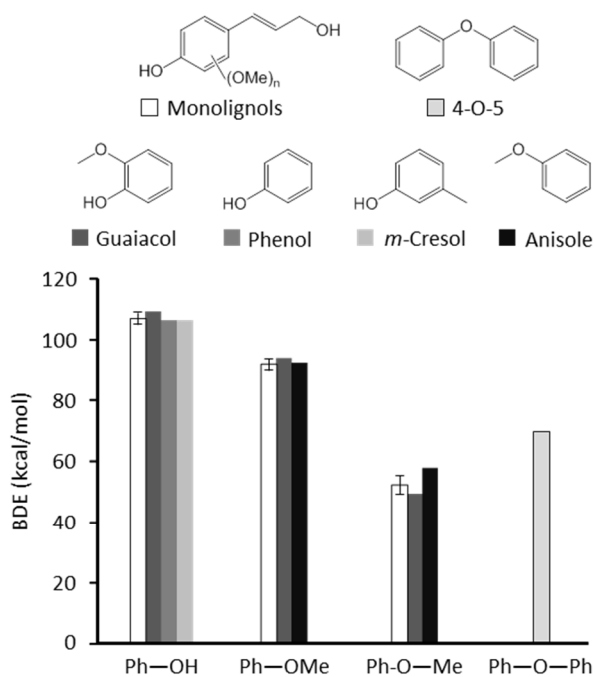


**Fig. 1** Comparison of the homolytic bond dissociation energies (BDEs) of monolignols and lignin-derived model compounds calculated by using the B3LYP/6-311+G(d,p) level of theory at 593 K in gas phase.

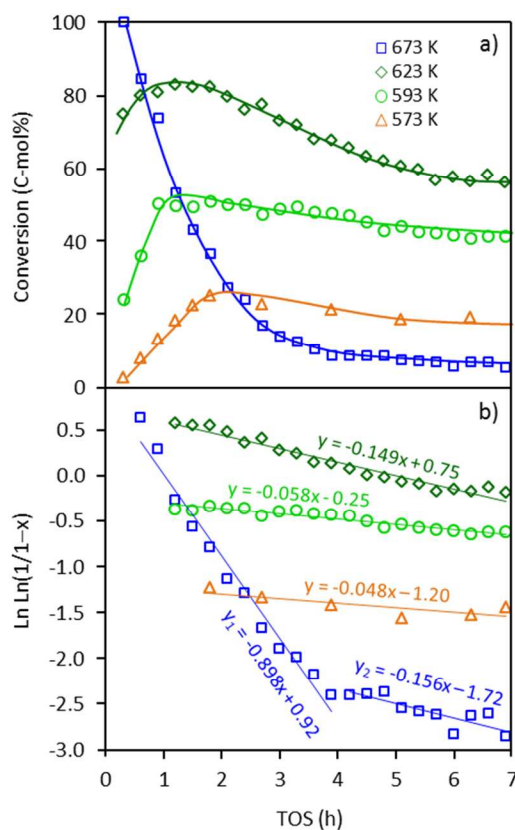


**Fig. 2** a) Conversion of *m*-cresol as a function of time-on-stream (TOS) at various reaction temperatures, and b) the corresponding catalyst deactivation profiles. Reaction conditions:  $P_{\text{Total}} = 1.013$  bar (0.015 bar  $P_{\text{Feed}}$ , balance  $H_2$ ),  $W/F = 0.035$  g<sub>Cat</sub> (mmol<sub>Feed</sub> h<sup>-1</sup>)<sup>-1</sup>, and no  $H_2$  pre-reduction.

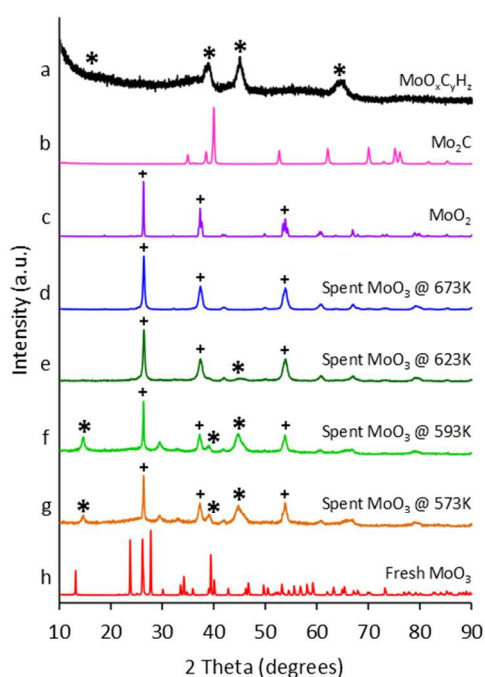


**Fig. 3** Normalised PXRD patterns of the spent  $\text{MoO}_3$  catalysts (in comparison with fresh  $\text{MoO}_3$ ,  $\text{MoO}_2$ ,  $\text{Mo}_2\text{C}$  and  $\text{MoO}_x\text{C}_y\text{H}_z$  samples) were measured at room temperature. The spent  $\text{MoO}_3$  samples derived from the experiments shown in Fig. 2 were passivated using 1 vol%  $\text{O}_2/\text{N}_2$  mixture at room temperature for 3 h prior to the analysis. The symbol (\*) and (+) indicates the peak assignment corresponding to  $\text{MoO}_x\text{C}_y\text{H}_z$  and  $\text{MoO}_2$  phases, respectively.

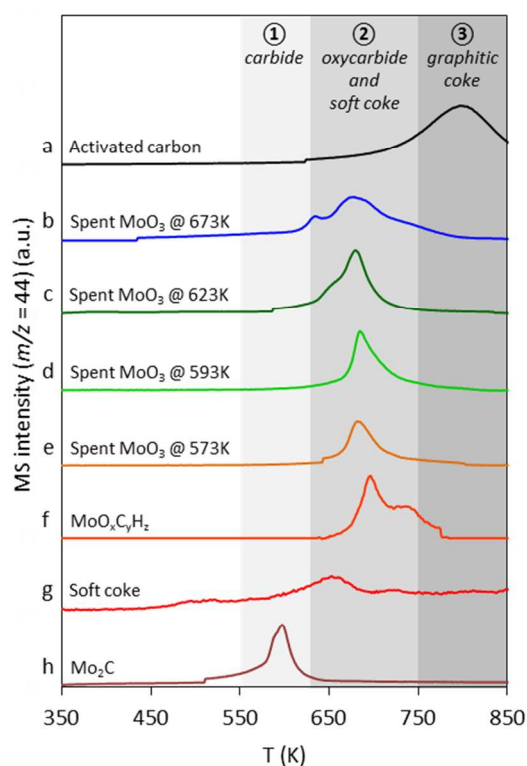


**Fig. 4** TGA-MS traces for the evolution of  $\text{CO}_2$  ( $m/z = 44$ ) from the spent  $\text{MoO}_3$  catalysts (in comparison with activated carbon, soft coke,  $\text{Mo}_2\text{C}$  and  $\text{MoO}_x\text{C}_y\text{H}_z$  samples). The spent  $\text{MoO}_3$  samples derived from the experiments shown in Fig. 2 were passivated using 1 vol%  $\text{O}_2/\text{N}_2$  mixture at room temperature for 3 h prior to the analysis. The soft coke sample was prepared by treating  $\text{MoO}_3$  with *m*-cresol under He at 593 K for 3 h.

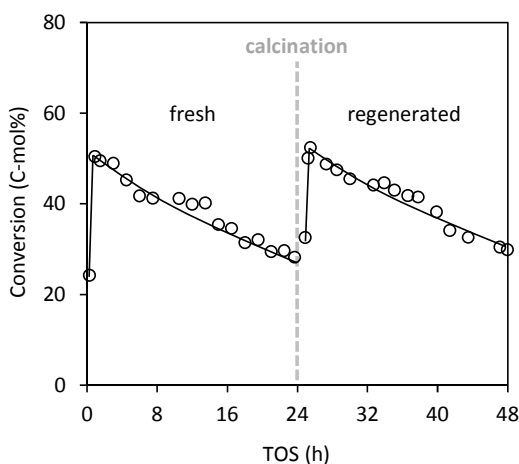


**Fig. 5** Regeneration of the  $\text{MoO}_3$  catalyst by calcination. The conversion of *m*-cresol was used as a probe reaction. Reaction conditions:  $T = 593 \text{ K}$ ,  $P_{\text{Total}} = 1.013 \text{ bar}$  ( $0.015 \text{ bar } P_{\text{Feed}}$ , balance  $\text{H}_2$ ),  $W/F = 0.035 \text{ g}_{\text{Cat}} (\text{mmol}_{\text{Feed}} \text{ h}^{-1})^{-1}$ , and no  $\text{H}_2$  pre-reduction. Regeneration conditions:  $T = 673 \text{ K}$ ,  $P_{\text{Total}} = 1.013 \text{ bar}$  ( $100\% \text{ O}_2$ ) for 3 h.

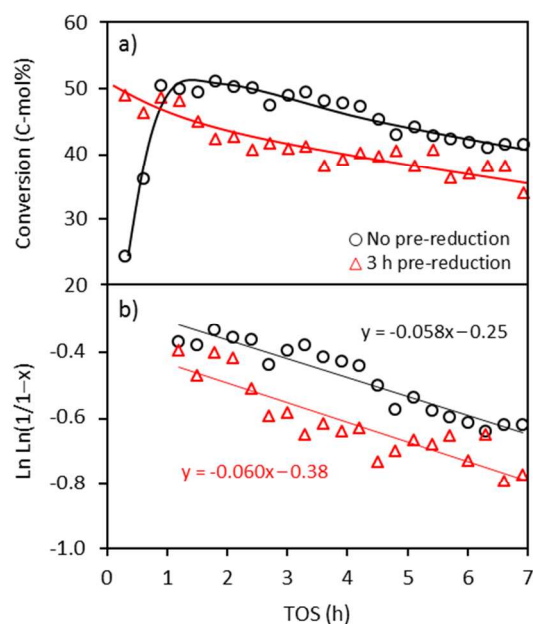


**Fig. 6** a) Effect of  $\text{H}_2$  pre-reduction of on the initial conversion of *m*-cresol using the  $\text{MoO}_3$  catalyst, and b) the corresponding catalyst deactivation profiles. Reaction conditions:  $T = 593 \text{ K}$ ,  $P_{\text{Total}} = 1.013 \text{ bar}$  ( $0.015 \text{ bar } P_{\text{Feed}}$ , balance  $\text{H}_2$ ), and  $W/F = 0.035 \text{ g}_{\text{Cat}} (\text{mmol}_{\text{Feed}} \text{ h}^{-1})^{-1}$ . Pre-reduction conditions:  $T = 593 \text{ K}$ ,  $P_{\text{Total}} = 1.013 \text{ bar}$  ( $100\% \text{ H}_2$ ) for 3 h.

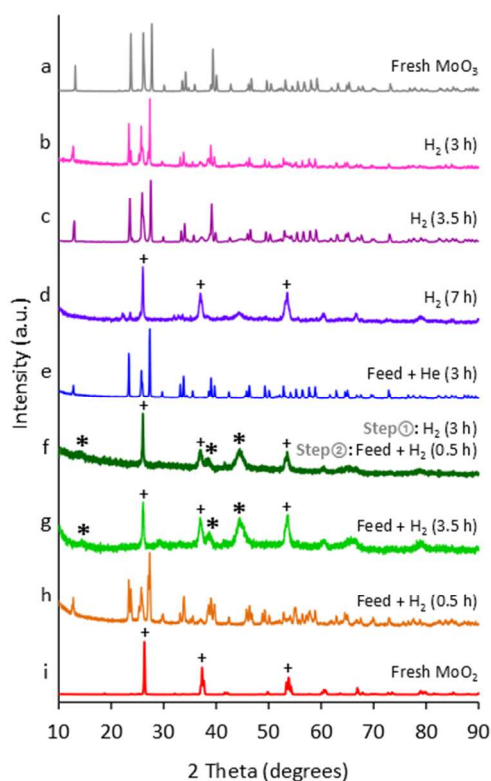


**Fig. 7** Effect of different pretreatments of the  $\text{MoO}_3$  catalyst. The normalised PXRD patterns were measured at room temperature. Pretreatment conditions: Feed = *m*-cresol (a carbon source),  $T = 593 \text{ K}$ ,  $P_{\text{Total}} = 1.013 \text{ bar}$  (100%  $\text{H}_2$  or He). Prior to the analysis, the samples were passivated using 1 vol%  $\text{O}_2/\text{N}_2$  mixture at room temperature for 3 h. The symbol (\*) and (+) indicates the peak assignment corresponding to  $\text{MoO}_x\text{C}_y\text{H}_z$  and  $\text{MoO}_2$  phases, respectively.

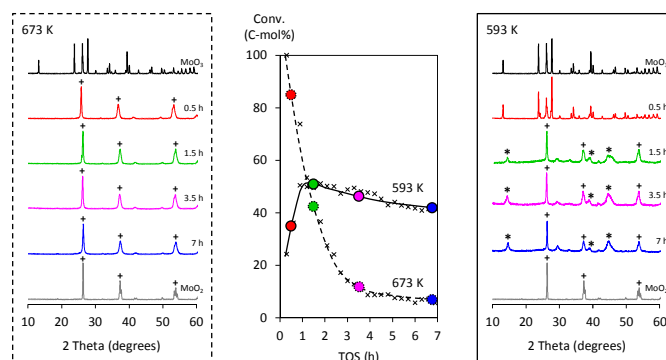


**Fig. 8** Phase evolution of  $\text{MoO}_3$  catalyst during the HDO of *m*-cresol at 673 K (left) and 593 K (right). The corresponding *m*-cresol conversion to toluene (>99% selectivity) was monitored up to 7 h (center). Reaction conditions:  $P_{\text{Total}} = 1.013 \text{ bar}$  ( $0.015 \text{ bar } P_{\text{Feed}}$ , balance  $\text{H}_2$ ),  $W/F = 0.035 \text{ g}_{\text{Cat}} (\text{mmol}_{\text{Feed}} \text{ h}^{-1})^{-1}$ , and no  $\text{H}_2$  pre-reduction. The catalyst samples were collected at various reaction times. Prior to the analysis, the samples were passivated using 1 vol%  $\text{O}_2/\text{N}_2$  mixture at room temperature for 3 h before performing the PXRD analysis. The symbol (\*) and (+) indicates the peak assignment corresponding to  $\text{MoO}_x\text{C}_y\text{H}_z$  and  $\text{MoO}_2$  phases, respectively.

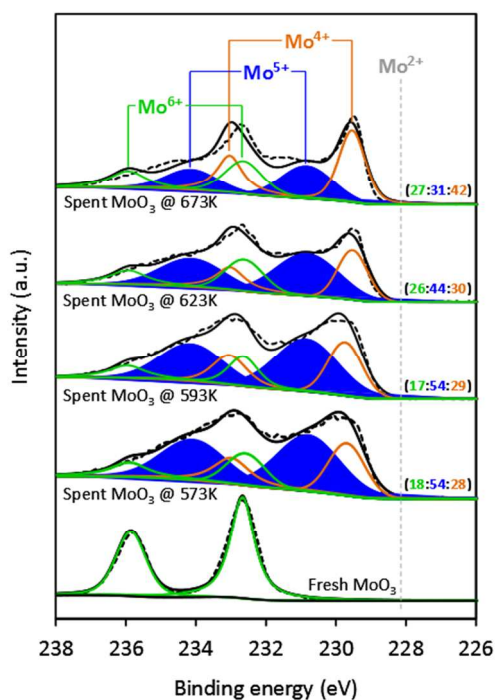


**Fig. 9** XPS of the Mo (3d) energy region of the fresh and spent MoO<sub>3</sub> samples derived from the experiments shown in Fig. 2. Prior to the analysis, the samples were passivated using 1 vol% O<sub>2</sub>/N<sub>2</sub> mixture at room temperature for 3 h. The numbers in parentheses are the corresponding oxidation state percentages of Mo<sup>6+</sup>, Mo<sup>5+</sup> and Mo<sup>4+</sup>, respectively.